

3D radiative transfer in η Carinae: application of the SIMPLEX algorithm to 3D SPH simulations of binary colliding winds

N. Clementel,¹★ T. I. Madura,² C. J. H. Kruip,¹ V. Icke¹ and T. R. Gull²

¹Leiden Observatory, Leiden University, PO Box 9513, NL-2300 RA Leiden, the Netherlands

²Astrophysics Science Division, Code 667, NASA Goddard Space Flight Center, Greenbelt, MD 20771, USA

Accepted 2014 June 24. Received 2014 June 20; in original form 2014 February 23

ABSTRACT

Eta Carinae is an ideal astrophysical laboratory for studying massive binary interactions and evolution, and stellar wind–wind collisions. Recent three-dimensional (3D) simulations set the stage for understanding the highly complex 3D flows in η Car. Observations of different broad high- and low-ionization forbidden emission lines provide an excellent tool to constrain the orientation of the system, the primary’s mass-loss rate, and the ionizing flux of the hot secondary. In this work, we present the first steps towards generating synthetic observations to compare with available and future *HST*/STIS data. We present initial results from full 3D radiative transfer simulations of the interacting winds in η Car. We use the SIMPLEX algorithm to post-process the output from 3D smoothed particle hydrodynamics (SPH) simulations and obtain the ionization fractions of hydrogen and helium assuming three different mass-loss rates for the primary star. The resultant ionization maps of both species constrain the regions where the observed forbidden emission lines can form. Including collisional ionization is necessary to achieve a better description of the ionization states, especially in the areas shielded from the secondary’s radiation. We find that reducing the primary’s mass-loss rate increases the volume of ionized gas, creating larger areas where the forbidden emission lines can form. We conclude that post-processing 3D SPH data with SIMPLEX is a viable tool to create ionization maps for η Car.

Key words: radiative transfer – binaries: close – stars: individual: Eta Carinae – stars: mass-loss – stars: winds, outflows.

1 INTRODUCTION

Eta Carinae (η Car) is an extremely luminous ($L_{\text{Total}} \gtrsim 5 \times 10^6 L_{\odot}$) colliding wind binary with a highly eccentric ($e \sim 0.9$), 5.54 yr orbit (Damineli, Conti & Lopes 1997; Davidson & Humphreys 1997; Hillier et al. 2001; Damineli et al. 2008a,b; Corcoran et al. 2010). η_A , the primary of the system, is our closest (2.3 ± 0.1 kpc; Smith 2006) example of a very massive star ($\sim 100 M_{\odot}$; Davidson & Humphreys 1997). A luminous blue variable, η_A has an extremely powerful stellar wind with $\dot{M}_{\eta_A} \approx 8.5 \times 10^{-4} M_{\odot} \text{ yr}^{-1}$ and $v_{\infty} \approx 420 \text{ km s}^{-1}$ (Hillier et al. 2001, 2006; Groh et al. 2012). Observations over the last two decades indicate that η_A ’s dense stellar wind interacts with the hotter, less-luminous companion star η_B and its much faster ($v_{\infty} \approx 3000 \text{ km s}^{-1}$; Pittard & Corcoran 2002), but much lower density ($\dot{M}_{\eta_B} \approx 10^{-5} M_{\odot} \text{ yr}^{-1}$), wind (Damineli et al. 2008b; Gull et al. 2009, 2011; Corcoran et al. 2010). These wind–wind interactions lead to various forms of time-variable emission and absorption seen across a wide range of wavelengths (Damineli et al. 2008b).

Observational signatures that arise as a result of the wind–wind interactions are important for studying η Car as they provide crucial information about the physical properties of the as-yet unseen η_B and the system as a whole. Three-dimensional (3D) hydrodynamical simulations show that the fast wind of η_B carves a low-density cavity out of the slower, denser inner wind of η_A for most of the orbit (Okazaki et al. 2008; Parkin et al. 2011; Madura & Groh 2012; Madura et al. 2012, 2013; Russell 2013). The same simulations indicate that the hot post-shock gas in the inner wind–wind interaction region (WWIR) gives rise to hard (up to 10 keV) X-ray emission that varies over the 5.54 yr period. Together with the models, spatially unresolved X-ray (Hamaguchi et al. 2007; Henley et al. 2008; Corcoran et al. 2010), optical (Damineli et al. 2008a,b), and near-infrared (Whitelock et al. 2004; Groh et al. 2010) observations have helped constrain the geometry and physical conditions within the inner WWIR.

In addition to the ‘current’ interaction between the two winds that occurs in the inner regions (at spatial scales comparable to the semimajor axis length $a \approx 15.4 \text{ au} \approx 0.0067 \text{ arcsec}$ at 2.3 kpc), larger scale ($\approx 3250 \text{ au} \approx 1.4 \text{ arcsec}$ in diameter) 3D hydrodynamical simulations exhibit outer WWIRs that extend thousands of au

★E-mail: clementel@strw.leidenuniv.nl

from the central stars (Madura et al. 2012, 2013, hereafter M12 and M13, respectively). Long-slit spectral observations of η Car with the *Hubble Space Telescope*/Space Telescope Imaging Spectrograph (*HST*/STIS) reveal these spatially-extended WWIRs, seen via emission from multiple low- and high-ionization forbidden lines (Gull et al. 2009, 2011; Teodoro et al. 2013).

Using a 3D dynamical model of the broad, extended [Fe III] emission observed in η Car by the *HST*/STIS, M12 confirmed the orbital inclination and argument of periastris that Okazaki et al. (2008) and Parkin et al. (2009) derived using X-ray data. More importantly, M12 broke the degeneracy inherent to models based solely on X-rays or other spatially-unresolved data and constrained, for the first time, the 3D orientation of η Car’s binary orbit. M12 find that the system has an argument of periastris $\omega \approx 240^\circ$ – 285° , with the orbital axis closely aligned with the Homunculus nebula’s polar axis at an inclination $i \approx 130^\circ$ – 145° and position angle on the sky $PA \approx 302^\circ$ – 327° , implying that apastron is on the observer’s side of the system and that η_B orbits clockwise on the sky. The dynamical model of M12 was based on 3D smoothed particle hydrodynamics (SPH) simulations of η Car’s colliding winds. A simple radiative transfer (RT) code was used to integrate the optically thin [Fe III] emission and generate synthetic slit-spectra for comparison to the available *HST*/STIS data. Although very successful, M12 used a semi-analytic approach to compute the volume of wind material photoionized by η_B . Furthermore, the fraction of Fe^{2+} as a function of T was estimated assuming collisional ionization equilibrium and available ion fraction data. Due to the lack, at the time, of a suitable code, proper 3D RT simulations of η_B ’s ionizing radiation were not performed. The location and strength of the [Fe III] emission was thus based on geometrical criteria, while in reality, the population of forbidden states depends on the local ionization state of the medium.

The goal of this paper is to improve considerably the modelling approach of M12 by computing full 3D RT simulations of the effects of η_B ’s ionizing radiation on η Car’s spatially-extended WWIRs. We accomplish this by applying the *SIMPLEX* algorithm for 3D RT on an unstructured Delaunay grid (Ritzerveld & Icke 2006; Ritzerveld 2007; Kruip et al. 2010; Paardekooper, Kruip & Icke 2010; Paardekooper et al. 2011) to recent 3D SPH simulations of η Car’s binary colliding winds (M13). We use *SIMPLEX* to obtain detailed ionization fractions of hydrogen and helium at the resolution of the original SPH simulations. This should allow us to predict much more precisely where, and to what extent, various observed forbidden emission lines form. This paper lays the foundation for future work aimed at generating synthetic spectral data cubes for comparison to data obtained with *HST*/STIS as part of a multicycle programme to map changes in η Car’s extended wind structures across one binary cycle from 2009 through 2015 (Gull et al. 2011; Teodoro et al. 2013). Comparison of the observations to the models should ultimately lead to more accurate constraints on the orbital, stellar, and wind parameters of the η Car system, such as η_A ’s mass-loss rate and η_B ’s temperature and luminosity (Mehner et al. 2010, 2012; M13).

While we focus specifically on the case of η Car, the numerical methods in this paper can be applied to numerous other colliding wind (e.g. WR 140, WR 137, WR 19; Fahed et al. 2011; Lefèvre et al. 2005; Williams, Rauw & van der Hucht 2009) and dusty ‘pinwheel’ (WR 104, WR 98a; Monnier, Tuthill & Danchi 1999; Tuthill, Monnier & Danchi 1999) binary systems. One of the biggest remaining mysteries is how dust can form and survive in such systems that contain a hot, luminous O star. Coupled with 3D hydrodynamical simulations, *SIMPLEX* simulations have the potential

to help determine the regions where dust can form and survive in these unique objects.

In the following section, we describe our numerical approach, including the SPH simulations, the *SIMPLEX* code, and the RT simulations. Section 3 describes the results. A discussion of the results and their implications follows in Section 4. Section 5 summarizes our conclusions and outlines the direction for future work.

2 CODES AND SIMULATIONS

2.1 The 3D SPH simulations

The hydrodynamical simulations were performed with the same SPH code used in M13, to which we refer the reader for details. Optically thin radiative cooling is implemented using the Exact Integration Scheme of Townsend (2009), with the radiative cooling function $\Lambda(T)$ calculated using *CLOUDY* 90.01 (Ferland et al. 1998) for an optically thin plasma with solar abundances. The pre-shock stellar winds and rapidly-cooling dense gas in the WWIR are assumed to be maintained at a floor temperature $= 10^4$ K due to photoionization heating by the stars (Parkin et al. 2011). The same initial wind temperature (T_{wind}) is assumed for both stars. The effect of T_{wind} on the flow dynamics is negligible (Okazaki et al. 2008).

Radiative forces are incorporated in the SPH code via an ‘anti-gravity’ formalism, the details of which can be found in M13 and Russell (2013). The individual stellar winds are parametrized using the standard ‘beta-velocity law’ $v(r) = v_\infty(1 - R_*/r)^\beta$, where v_∞ is the wind terminal velocity, R_* the stellar radius, and β (set = 1) a free parameter describing the steepness of the velocity law. Effects due to ‘radiative braking’ (Gayley, Owocki & Cranmer 1997; Parkin et al. 2011), photospheric reflection (Owocki 2007), and self-regulated shocks (in which ionizing X-rays from the WWIR inhibit the wind acceleration of one or both stars, leading to lower pre-shock velocities and lower shocked plasma temperatures; Parkin & Sim 2013), are not included. These effects are not expected to play a prominent role in η Car at the orbital phases near apastron considered in this work (Parkin et al. 2009, 2011; Russell 2013; M13). We include the more important velocity-altering effects of ‘radiative inhibition’, in which one star’s radiation field reduces the net rate of acceleration of the opposing star’s wind (Stevens & Pollock 1994; Parkin et al. 2009, 2011). However, because we fix the mass-loss rates in our anti-gravity approach, possible changes to the mass-loss due to radiative inhibition are not included. These changes are not expected to be significant in η Car and should not greatly affect our results or conclusions (M13).

Using an *xyz* Cartesian coordinate system, the binary orbit is set in the *xy* plane, with the origin at the system centre of mass and the major axis along the *x*-axis. The two stars orbit counter-clockwise when viewed from the *+z*-axis. By convention, $t = 0$ ($\phi = t/204 = 0$) is defined as periastron. Simulations are started at apastron and run for multiple consecutive orbits. Orbits are numbered such that $\phi = 1.5, 2.5$ and 3.5 correspond to apastron at the end of the second, third and fourth full orbits, respectively.

The outer spherical simulation boundary is set at $r = 100a$ from the system centre of mass, where $a = 15.45$ au is the length of the orbital semimajor axis. Particles crossing this boundary are removed from the simulations. The computational domain is comparable in size to past and planned *HST*/STIS mapping observations of the interacting stellar winds in η Car’s central core ($\sim \pm 0.67$ arcsec $\simeq \pm 1540$ au; Gull et al. 2011; M12; Teodoro et al. 2013). As demonstrated by Gull et al. (2011) and M12,

Table 1. Stellar, wind and orbital parameters of the 3D SPH simulations.

Parameter	η_A	η_B	Reference
M_* (M_\odot)	90	30	H01; O08
R_* (R_\odot)	60	30	H01; H06
T_{wind} (10^4 K)	3.5	3.5	O08; M13
\dot{M} ($10^{-4} M_\odot \text{ yr}^{-1}$)	8.5, 4.8, 2.4	0.14	G12; P09
v_∞ (km s^{-1})	420	3000	G12; P02
P_{orb} (d)	2024		D08a
e	0.9		C01; P09
a (au)	15.45		C01; O08

Notes. M_* and R_* are the stellar mass and radius. T_{wind} is the initial wind temperature. \dot{M} and v_∞ are the stellar-wind mass-loss rate and terminal speed, respectively. P_{orb} is the period, e is the eccentricity, and a is the length of the orbital semimajor axis.

References: C01 = Corcoran et al. (2001); H01 = Hillier et al. (2001); P02 = Pittard & Corcoran (2002); H06 = Hillier et al. (2006); D08a = Damineli et al. (2008a); O08 = Okazaki et al. (2008); P09 = Parkin et al. (2009); G12 = Groh et al. (2012).

3D simulations at this scale are necessary for understanding and modelling the extended, time-variable forbidden line emission structures that are spatially and spectrally resolved by *HST*/STIS.

The total number of SPH particles used in the simulations is roughly between 5×10^5 and 9×10^5 , depending on the value of \dot{M}_{η_A} . The adopted simulation parameters (Table 1) are consistent with those derived from the available observations, although there has been some debate on the exact present day value of \dot{M}_{η_A} (see M13 for details). In an effort to better constrain η_A 's current \dot{M} , M13 performed multiple 3D SPH simulations assuming different \dot{M}_{η_A} . We use the same naming convention as M13 when referring to the simulations in this paper for the different \dot{M}_{η_A} , namely, Case A ($\dot{M}_{\eta_A} = 8.5 \times 10^{-4} M_\odot \text{ yr}^{-1}$), Case B ($\dot{M}_{\eta_A} = 4.8 \times 10^{-4} M_\odot \text{ yr}^{-1}$), and Case C ($\dot{M}_{\eta_A} = 2.4 \times 10^{-4} M_\odot \text{ yr}^{-1}$). We discuss the effects of the three values of \dot{M}_{η_A} on the RT calculations in Section 3.2.

2.2 The SIMPLEX algorithm for RT on an unstructured mesh

The SIMPLEX algorithm, conceived by Ritzerveld & Icke (2006), implemented by Ritzerveld (2007), and further improved by Paardekooper et al. (2010) and Kruip et al. (2010), is designed to solve the general equations of particle transport by expressing them as a walk on a graph. At the basis of the method lies the unstructured grid on which the photons are transported. A given medium (e.g. a density or optical-depth field) is typically sampled with a Poisson point process and the resulting point distribution is used to tessellate space according to the Voronoi recipe: all points in a cell are closer to the nucleus of that cell than to any other nucleus. The Voronoi nuclei are then connected by a Delaunay triangulation. The grid is constructed to describe the properties of the underlying physical medium, through which the photons travel, in such a way that more grid points are placed in regions with a higher opacity. The result is a higher resolution in places where it is needed most, i.e. where the optical depth is highest.

Photons are transported from node to node along the edges of the Delaunay triangulation, where each transition has a given probability. In one computational cycle, every nucleus in the grid transports its content to neighbouring nuclei, optionally absorbing or adding photons. Which neighbours are selected for transport depends on

the specific process. Even though SIMPLEX was originally developed for application in cosmological RT, its properties are still well suited for our purpose.

In Section 2.2.1, we present the construction procedure for the SIMPLEX RT mesh starting from the SPH particle distribution. Section 2.2.2 describes the processes that determine the ionization state of the gas, such as collisional- and photoionization and recombination, plus the specifics of their implementation in SIMPLEX (for further details see chapters 4 and 5 of Kruip 2011).

2.2.1 Grid construction

The 3D SPH simulations provide the time-dependent 3D density, temperature, and velocity structure of η Car's interacting winds on the spatial scales of interest, thus forming the basis of our model. As in M12, the RT calculations are performed as post-processing of the 3D SPH output. The hydrodynamic influence of the radiation on the gas is thereby neglected. We do not expect this to have a very large influence on the results since the material photoionized by η_B responds nearly instantaneously to its UV flux, i.e. the recombination time-scale is very small relative to the orbital time-scale, especially around apastron (M12).

The first step is to convert the SPH particle distribution to a SIMPLEX mesh. Since the density field is given by discrete particles, we might obtain an estimate of the density at any position in the domain using a typical SPH kernel function $W(r, h)$ with

$$\rho(r) = \sum_j m_j W(|r - r_j|, h_j), \quad (1)$$

where h is the smoothing length and m_j is the mass of particle j . Using this kernel function one can then sample the data using the sampling functions described in e.g. Paardekooper et al. (2010) and Kruip et al. (2010). However, given the fact that the original data are already particle-based, it is more natural for us to use the SPH particles themselves as the generating nuclei for the Voronoi–Delaunay mesh. This leads to a more direct estimate of the density, given by the division of the particle mass by the Voronoi volume of its corresponding cell. Another advantage is that, due to pressure forces, the particles in an SPH simulation are in general positioned more regularly than for a pure Poisson process. Finally, we note that with future applications of 3D time-dependent radiation-hydrodynamics in mind, a coupling of SIMPLEX with an SPH method is most natural when the radiation transport is applied directly to the SPH particles so that no spurious interpolation is needed. For these reasons, we use every SPH particle as the nucleus of a Voronoi cell. This procedure yields density estimates that are less smooth than those obtained with typical kernel functions of the type of equation (1), but guarantees mass conservation and represents small-scale structures in the density field more accurately.

Fig. 1 presents an example of the resulting SIMPLEX mesh and number density at apastron for a typical 3D SPH simulation of η Car. The first row shows the original number density from the SPH simulation for slices in the xy , xz , and yz planes for the Case A simulation. The SIMPLEX mesh (second row) reproduces everywhere the features present in the original SPH data. The resulting SIMPLEX number density (third row) follows extremely well the SPH one in shape, resolution, and value.

Paardekooper et al. (2010) and Kruip et al. (2010) discussed how undersampling can have a negative effect on the outcome of an RT simulation that uses grid-based data. In principle, the same problem holds for particle-based data in areas where sharp gradients are present in the number density of SPH particles. To ensure that

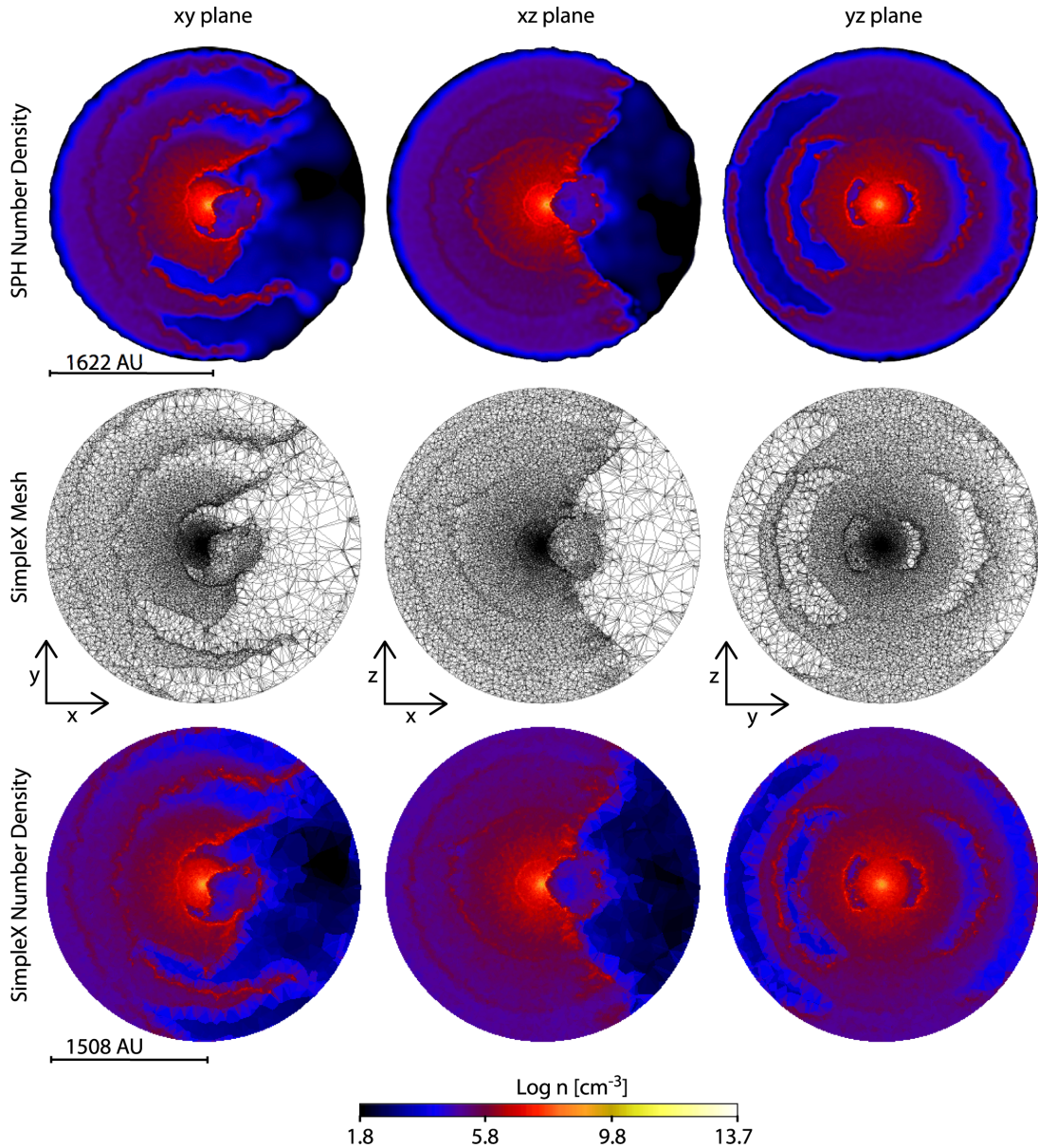


Figure 1. Slices in the xy (left-hand column), xz (middle column) and yz (right-hand column) planes through the 3D simulation volume for the Case A simulation at apastron. Rows show, from top to bottom, the original SPH number density distribution (log scale, cgs units), the SIMPLEX mesh, and the resulting SIMPLEX number density (same log scale, cgs units). The resolution of the SIMPLEX mesh, as well the number density, follow well the resolution of the original SPH data. In the first column (i.e. the orbital plane), η_A is to the left and η_B is to the right. The length scales are shown under the top and bottom left-hand panels. Note that the domain size in the SIMPLEX snapshots is slightly smaller than that of the SPH simulations only because we have, for visualization purposes, removed the border points used to generate the SIMPLEX mesh.

our results are not prone to such issues, we developed a method to increase the resolution of any sparsely sampled regions. We begin with the triangulation of the SPH particles. For every tetrahedron in this triangulation that is larger than a tolerance volume, an additional vertex is placed in the centre of the tetrahedron, and $1/5$ of the mass of the four vertices that constitute the tetrahedron is given to the new vertex. This procedure is manifestly mass conserving and regularizes the mesh in low-resolution regions.

To study the influence this procedure has on the RT results, we performed test RT simulations with and without resolution enhancements in normally sparsely-sampled regions. For these tests, we used a characteristic η Car SPH simulation snapshot in which the densities span roughly ten orders of magnitude (i.e. the top row of

Fig. 1). If the RT results are sensitive to sharp gradients, we expect significant differences between the RT simulation with increased resolution and the original non-enhanced simulation.

Although the difference is not large, the overall density in the affected regions is slightly enhanced by the new interpolation. However, we find that the overall shape and spatial extent of the ionized regions does not change. The ionization fraction in the local region most affected by the increased resolution is somewhat lower after the procedure though. This is consistent with the notion that the interpolation increases slightly the density in the higher resolution region, resulting in a slightly higher recombination rate. The difference, however, is negligible. These results suggest that locally increasing the resolution does not change the overall shape and size

of the ionized regions. We are therefore confident that our RT results are not susceptible to systematic effects related to strong gradients in the SPH particle number density (for further detail see chapters 3 and 4 of Kruip 2011).

2.2.2 Ionization state and chemistry of the gas

In a gas with cross-section for photoionization $\sigma(\mathbf{x}, \nu)$ at position \mathbf{x} , the local photoionization rate, $\Gamma_{P,i}(\mathbf{x})$ (which gives the number of photoionizations per second per atom of species i in units $[s^{-1}]$), is given by (Osterbrock & Ferland 2006):

$$\Gamma_{P,i}(\mathbf{x}) \equiv \int_0^\infty \frac{4\pi J_\nu(\mathbf{x})}{h\nu} \sigma_i(\mathbf{x}, \nu) d\nu, \quad (2)$$

where $J_\nu(\mathbf{x})$ is the local mean intensity and the three species capable of absorbing ionizing photons in the code are H I, He I and He II. For simplicity, we only consider the ionization of hydrogen and helium atoms. Implementing ionization processes in a numerical code requires that the relevant equations be expressed in a discretized form. In particular, we need to know the ionization rate per species in each cell of our computational grid. In *SIMPLEX*, ionizing radiation travels from cell to cell along the Delaunay edges. At the nucleus of each Voronoi cell, photons are taken away from the incoming radiation field and their energy is used to ionize the neutral atoms of that Voronoi cell. Given the number densities of these species ($n_{\text{H I}}$, $n_{\text{He I}}$ and $n_{\text{He II}}$), and the path length through the cell l , the monochromatic optical depth of ionizing radiation τ_ν is

$$\tau_\nu \equiv (n_{\text{H I}}\sigma_{\text{H I}} + n_{\text{He I}}\sigma_{\text{He I}} + n_{\text{He II}}\sigma_{\text{He II}})l. \quad (3)$$

The total number of ionizations per unit time, \dot{N}_{ion} for a cell with optical depth τ_ν is then given by

$$\dot{N}_{\text{ion}} = \int_0^\infty \dot{N}_\nu(\nu) [1 - \exp(-\tau_\nu)] d\nu, \quad (4)$$

where $\dot{N}_\nu(\nu)$ is the number of ionizing photons per unit time streaming into the cell. To quantify how much of the resulting ionizations is due to a particular species, we use the contribution to the total optical depth of that species. The number of ionizations of species i per unit time is

$$\dot{N}_{\text{ion},i} = \dot{N}_{\text{ion}} \int_0^\infty \frac{\tau_{\nu,i}}{\tau_\nu} d\nu. \quad (5)$$

Dividing by the number of neutral atoms of species i in the cell, N_i , then gives the spatially discretized equivalent of equation (2)

$$\Gamma_{P,i} = \frac{\dot{N}_{\text{ion},i}}{N_i}. \quad (6)$$

In numerical simulations involving radiation, it is often necessary to approximate the continuous spectrum of radiation with a finite number of discrete frequency bins due to memory requirements. The extreme (but often employed) limit of one single frequency bin is commonly referred to as the ‘grey approximation’. Although in the grey approximation all spectral information is lost, it is still possible to enforce the conservation of a quantity of importance such as the number of ionizations per unit time or the energy deposition into the medium per unit time. For simplicity, we employ the grey approximation in this work.

The conservation of ionizations is accomplished by defining the effective cross-section for species i , $\sigma_{I,i}$, as

$$\sigma_{I,i} = 4\pi \int_0^\infty \frac{\sigma_i(\nu) J_\nu}{h\nu} d\nu / \dot{N}, \quad (7)$$

where \dot{N} is the rate of ionizing photons per surface area defined by

$$\dot{N} \equiv 4\pi \int_0^\infty \frac{J_\nu}{h\nu} d\nu. \quad (8)$$

The photoionization rate is thus given by

$$\Gamma_{P,i} = \sigma_{I,i} \dot{N}. \quad (9)$$

In addition to photoionization, we include collisional ionization due to the interaction of free electrons and neutral atoms. As this is a kinetic process, the collisional ionization rate, Γ_C , depends on the thermal state of the electrons and is given by

$$\Gamma_C = n_e \sum_i \Gamma_i(T) n_i, \quad (10)$$

where $\Gamma_i(T)$ are the collisional ionization rates and n_e is the electron number density. The total ionization rate is the sum of photo- and collisional ionization rates, $\Gamma = \Gamma_P + \Gamma_C$.

The inverse process of ionization is recombination. This free-bound interaction of electrons and ions depends on temperature and number density of ions and electrons. The number of recombinations per unit time per hydrogen atom $[s^{-1}]$ is

$$R_i = n_e \alpha_i(T), \quad (11)$$

where $\alpha_i(T)$ is the recombination coefficient of species i .

We note that we use the ‘case B’ recombination coefficient where the recombination transition to the ground-state is excluded under the assumption that the radiation associated with this transition is absorbed nearby, resulting in a new ionization. This is referred to as the ‘on-the-spot’ approximation. Details on the implementation of these processes, as well as the various rates and cross-sections used can be found in chapter 5 of Kruip (2011).

Together, ionizations and recombinations determine the ionization-state of the gas, described by the following three coupled differential equations and three closure relations

$$\begin{aligned} \dot{n}_{\text{H I}} &= n_{\text{H II}} R_{\text{H II}} - n_{\text{H I}} \Gamma_{\text{H I}} \\ \dot{n}_{\text{He I}} &= n_{\text{He II}} R_{\text{He II}} - n_{\text{He I}} \Gamma_{\text{He I}} \\ \dot{n}_{\text{He II}} &= n_{\text{He III}} R_{\text{He III}} - n_{\text{He II}} \Gamma_{\text{He II}} \\ n_{\text{H}} &= n_{\text{H I}} + n_{\text{H II}} \\ n_{\text{He}} &= n_{\text{He I}} + n_{\text{He II}} + n_{\text{He III}} \\ n_e &= n_{\text{H II}} + n_{\text{He II}} + 2n_{\text{He III}}. \end{aligned} \quad (12)$$

This set of equation does not have a general analytical solution and must be solved numerically. For this purpose, we adopt the sub-cycling scheme described in Pawlik & Shaye (2008). In this scheme, ionizations and recombinations are evolved on a time-scale that is smaller than the ionization or recombination time-scales t_{ion} and t_{rec} . During a RT time-step, the ionizing flux is assumed to be constant, making the procedure manifestly photon-conserving. This allows for radiative time-steps Δt_{rt} that are much larger than the dominant time-scale governing the evolution of the ionization state. The sub-cycling time-step for both ionization and recombination is

$$\Delta t_{\text{sub}} \equiv \frac{t_{\text{ion}} t_{\text{rec}}}{t_{\text{ion}} + t_{\text{rec}}}. \quad (13)$$

Because the procedure is analogous for each species, we give here only the explicit example for the integration step for hydrogen. At time $t_{\text{sub}} \in (t_{\text{rt}}, t_{\text{rt}} + \Delta t_{\text{rt}})$ the rate equation is given by

$$dn_{\text{H II}}^{(t_{\text{sub}})} = n_{\text{H I}}^{(t_{\text{sub}})} \Gamma_{\text{H}}^{(t_{\text{sub}})} \Delta t_{\text{sub}} - n_e^{(t_{\text{sub}})} n_{\text{H II}}^{(t_{\text{sub}})} \alpha_{\text{H}}(T) \Delta t_{\text{sub}}, \quad (14)$$

where the photoionization rate at t_{sub} is

$$\Gamma_{\text{H}}^{(t_{\text{sub}})} = \Gamma_{\text{H}} \left(\frac{1 - e^{-\tau^{(t_{\text{sub}})}}}{1 - e^{-\tau}} \right) \frac{n_{\text{H I}}}{n_{\text{H I}}^{(t_{\text{sub}})}}, \quad (15)$$

where Γ_{H} and τ are the photoionization rate and optical depth at the beginning of the sub-cycling and $\tau^{(t_{\text{sub}})} = \tau n_{\text{H I}}^{(t_{\text{sub}})}/n_{\text{H I}}$. By defining the photoionization rate in this way, the ionizing flux in the cell is constant during the RT time-step. This sub-cycling scheme becomes computationally expensive when $\Delta t_{\text{sub}} \ll \Delta t_{\text{rt}}$, but photoionization equilibrium is generally reached after a few sub-cycles. It is then no longer necessary to explicitly integrate the rate equation, but instead use the values of the preceding sub-cycle step. This way of sub-cycling ensures photon conservation even for large RT time-steps.

2.3 Application of SIMPLEX to η Car

Since the SIMPLEX calculations are performed as post-processing on the 3D SPH simulation output, we use snapshots corresponding to an orbital phase of apastron (Fig. 1). The reason for this choice lies in the slow dynamical changes that the system undergoes around apastron. This ‘stable’ situation allows us to run RT simulations for a sufficiently long time without worrying about important changes to the 3D structure of the system that occur around periastron (Okazaki et al. 2008; Parkin et al. 2011; M12, M13). Moreover, the *HST*/STIS mapping data currently in-hand to be modelled was taken at phases around apastron during η Car’s orbital cycle (Gull et al. 2011; Teodoro et al. 2013). Detailed modelling of future (late 2014 through early 2015) *HST* observations obtained across η Car’s periastron event is deferred to future work.

We focus on the ionization of H and He due to η_{B} , assuming the same abundance by number of He relative to H as Hillier et al. (2001), $n_{\text{He}}/n_{\text{H}} = 0.2$. The reasons for this single-source approximation are discussed in Section 2.3.1. We performed tests to determine the correct time-step for accurate RT calculations of the ionization volumes and fractions, and find that a simulation time-step of ~ 3 s is required. The SPH output is post-processed with SIMPLEX until the ionization state reaches an equilibrium value. This typically happens within ~ 3 months for the SPH snapshots investigated. We thus set the total SIMPLEX simulation time to three months. Because the gas is assumed to be initially almost fully neutral, this provides an upper limit on the time it takes before convergence is reached. Since this limit is well within the orbital time-scale around apastron, this is another indication that post-processing of the SPH simulations does not significantly alter our results.

2.3.1 Influence of the primary star η_{A}

Detailed fitting of the optical and UV spectra of η Car by Hillier et al. (2001, 2006) and Groh et al. (2012) shows that for $\dot{M}_{\eta_{\text{A}}} \approx 8.5 \times 10^{-4} M_{\odot} \text{ yr}^{-1}$, the region of fully ionized H around η_{A} extends radially ~ 120 au, while the region of doubly-ionized He extends ~ 0.7 au, and that of singly-ionized He from ~ 0.7 to 3 au. Assuming a constant spherical mass-loss rate, the density in the η_{A} wind is expected to fall off as r^{-2} . To explore the dependence of the position of the ionization fronts on the ionizing luminosity of η_{A} , we performed 1D calculations using an equilibrium chemistry solution, where the ionization fractions of hydrogen and helium are set to their equilibrium values under the assumption that the incoming flux of ionizing photons is constant. As mentioned in Section 2.2.2, the ionization state of the gas is described by the first three equations

in set (12). We can derive the equilibrium equations by setting $\dot{n}_{\text{H I}} = \dot{n}_{\text{He I}} = \dot{n}_{\text{He II}} = 0$. After some algebra this yields

$$\begin{aligned} x_{\text{H I}} &= (1 + \Gamma_{\text{H I}}/R_{\text{H I}})^{-1} \\ x_{\text{H II}} &= 1 - x_{\text{H I}} \\ x_{\text{He I}} &= [1 + \Gamma_{\text{He I}}/R_{\text{He II}} \times (1 + \Gamma_{\text{He II}}/R_{\text{He III}})]^{-1} \\ x_{\text{He II}} &= x_{\text{He I}} \Gamma_{\text{He I}}/R_{\text{He II}} \\ x_{\text{He III}} &= x_{\text{He II}} \Gamma_{\text{He II}}/R_{\text{He III}}, \end{aligned} \quad (16)$$

where x_i is the fraction of species i and we have used $n_i = x_i n_j$ where $j \in (\text{H}, \text{He})$. These equations are coupled by the free electron density given by the last equation in (12).

Unfortunately, the set of equations (16) cannot be solved analytically due to the non-linear dependence on ionization fractions of the photoionization rate through the optical depth. More specifically, the photoionization rate in a cell is given by equation (6), where the monochromatic analog of equation (4) is

$$\dot{N}_{\text{ion}} = \dot{N}_{\gamma} [1 - \exp(-\tau)], \quad (17)$$

with $\tau = (x_{\text{H I}} n_{\text{H}} \sigma_{\text{H I}} + x_{\text{He I}} n_{\text{He}} \sigma_{\text{He I}} + x_{\text{He II}} n_{\text{He}} \sigma_{\text{He II}}) l$. Because of this non-linear dependence, the equilibrium fractions must be solved iteratively. If the iterative procedure converges, the neutral fractions are assigned to the cell under treatment and the flux is diminished by the number of absorptions during that time-step Δt ($n_{\text{H I}} \Gamma_{\text{H I}} \Delta t$).

The density profile used in the 1D code is obtained from the expression $\rho(r) = \dot{M}_{\eta_{\text{A}}}/4\pi r^2 v(r)$, where $v(r) = v_{\infty}(1 - R_{\ast}/r)^{\beta}$ (see M13, equation A1). The 1D code simulates radiation travelling through spherically symmetric shells with a maximal radius of the simulation, ~ 1622 au. The radiation is injected in the first shell and then travels outwards until it is either absorbed or exits the last shell. For the results shown we used $\sim 3 \times 10^4$ shells. We note that time-stepping is arbitrary because of the equilibrium chemistry. The only variable is therefore the luminosity of the source η_{A} .

Using $\dot{M}_{\eta_{\text{A}}} \approx 8.5 \times 10^{-4} M_{\odot} \text{ yr}^{-1}$, for luminosities below a critical value ($1.9 \times 10^{53} \text{ s}^{-1}$), the computational box is neutral and the Strömgren radii are confined to the central 0.7 au (top panel, Fig. 2). The H ionization front is located somewhere between the centre and the outside of the box for a very small range of luminosity values (centred around $1.91756 \times 10^{53} \text{ s}^{-1}$, centre panel, Fig. 2). The slightest increase in luminosity results in a completely ionized box, while further increase results only in a lower neutral fraction throughout the simulation volume (bottom panel, Fig. 2). This behaviour is completely expected, however, for ionization fronts in power-law density profiles with powers less than $-2/3$ (Franco, Tenorio-Tagle & Bodenheimer 1990; Shapiro et al. 2006). For such profiles, the circumstellar medium simply cannot support stable ionization fronts.

For these reasons, constraining the ionization fronts in η_{A} ’s wind to the values derived by Hillier et al. (2001, 2006) and Groh et al. (2012) using SIMPLEX is practically impossible given the fronts’ intrinsically unstable nature. We realize this 1D result is oversimplified since the instability is real in a pure H or H + He gas, but will disappear with the introduction of the myriad of spectral lines, mostly by Fe, that have a so-called ‘line blanketing’ effect on the stellar spectra. However, the inclusion of such additional species and blanketing effects is beyond the scope of this paper.

Given the above difficulties, the most sensible choice for an initial effort to model the ionized WWIRs is to omit η_{A} ’s radiation altogether. This may seem an oversimplification at first, but there are several arguments for this approximation. First, for the high $\dot{M}_{\eta_{\text{A}}}$ Case A and B simulations, 1D CMFGEN models by Hillier et al. (2001, 2006) show that the primary source will sustain an ionized

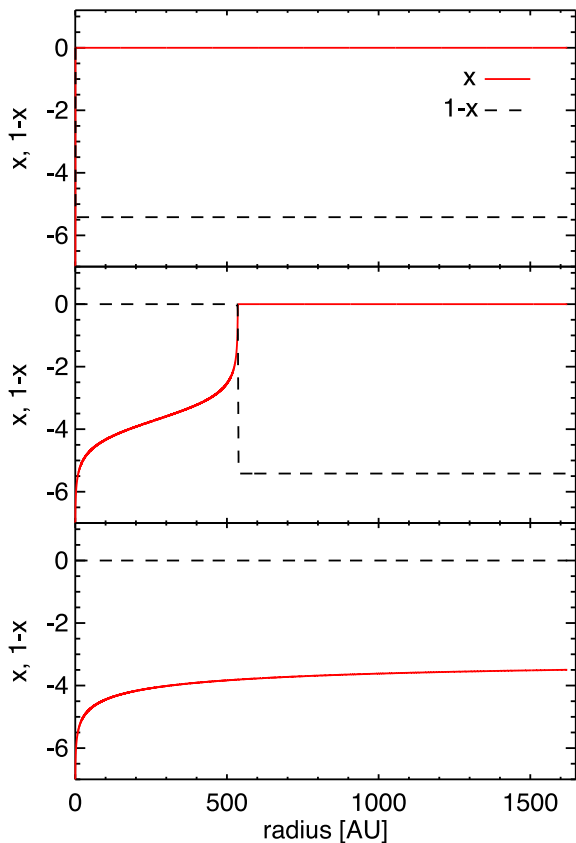


Figure 2. Neutral (x , solid lines) and ionized ($1 - x$, dashed lines) fractions of H (log scale) as a function of distance for the 1D RT simulations of η_A described in Section 2.3.1 and luminosities of Top: $1.9 \times 10^{53} \text{ s}^{-1}$, Centre: $1.91756 \times 10^{53} \text{ s}^{-1}$, and Bottom: $1.91758 \times 10^{53} \text{ s}^{-1}$. This behaviour signifies that the H ionization front is highly unstable and thus changes qualitatively with small perturbations in either the density or the luminosity.

hydrogen region that spans roughly 240–260 au in diameter, $\sim 0.04 - 0.05$ per cent of the volume of the SPH and SIMPLEX simulations. The same models show that the total sum volume of singly plus doubly ionized helium in the central η_A wind accounts for $\sim 10^{-6}$ per cent and 10^{-5} per cent of the SIMPLEX simulation volume for Cases A and B, respectively. These volumes are too close to the primary and too small to directly affect the ionization fronts and fractions at the locations where the spatially-extended, high-velocity forbidden line emission forms, especially at orbital phases near apastron (Gull et al. 2009, 2011; M12; M13). They may, however, influence the ionization structure further away indirectly by reducing the opacity for photons from the secondary source. This may be especially true very close to periastron. We expect that this would primarily result in UV flux from η_A penetrating the WWIR more easily, effectively increasing the ionized fraction on the far side of the primary source. For an observer on Earth though, this region is, at periastron, located behind η_A and therefore likely obscured by the dense primary wind.

Secondly, although extremely luminous, because it is enshrouded by a dense, optically-thick wind, η_A has a spectrum representative of a much cooler star than η_B (Hillier et al. 2001, 2006). The effective temperature of η_A at optical depth $\tau = 2/3$ ($r \approx 4$ au) is predicted to be ~ 9200 K for Cases A and B (Hillier et al. 2001, 2006). The ionizing flux from η_A is thus substantially diminished before reaching the WWIR, located ~ 20 – 22 au from η_A when the system is near apastron. Since essentially zero photons with energies above 13.6 eV from η_A reach the WWIRs on the apastron side of the system

at times near apastron, omission of the η_A source is a justifiable simplification when the focus is on forbidden emission lines with ionization potentials above 13.6 eV.

One might try to argue that because the ionized hydrogen and helium volumes in the inner primary wind extend far enough to encompass both stars and the WWIR at phases close to periastron, photons from η_A will also reach the apastron side of the simulation volume. This argument relies, however, on the assumption that the ionized regions are indeed spherical and therefore penetrate the WWIR towards the secondary star. This assumption is likely incorrect given the high density of the WWIR. In other words, we would be applying a model based on spherical symmetry to a region that clearly has a very asymmetrical geometry.

The exception to the above arguments is the Case C simulation. In this instance, according to 1D CMFGEN models (Hillier et al. 2006; M13), H is fully ionized in the pre-shock η_A wind throughout the entire simulation domain. Moreover, the He II region in the inner η_A wind extends radially ~ 120 au. While neglecting the η_A ionizing source in this case likely produces incorrect RT results in the regions of η_A wind on the periastron side of the system, for our purposes, the situation is actually not so bad. First, we note that, based on previous works, the mass-loss rate of η_A is very likely not as low as the value assumed in the Case C situation (see arguments in e.g. Hillier et al. 2006; Parkin et al. 2009; Teodoro et al. 2012, 2013; Russell 2013; M12; M13), and so we will not be using the SIMPLEX results obtained here for Case C to model the observed broad, high-ionization forbidden line emission. Rather, in addition to investigating how a reduced \dot{M}_{η_A} affects the ionization structure on the apastron side of the system, we use Case C as an illustrative example to determine whether η_B 's ionizing radiation can penetrate the dense WWIRs and further affect the ionization state of η_A 's wind. Having H initially ionized in the pre-shock η_A wind would primarily influence the ionization structure indirectly by reducing the opacity for photons from η_B (assuming they can penetrate the WWIR), increasing the ionized fraction of H in the pre-shock η_A wind, but having little effect on the overall ionization volume.

Regarding the He ionization structure in Case C, because the inner He II region extends ~ 120 au, the innermost WWIR penetrates η_A 's He II zone, even at apastron. However, the total volume of this inner He II region is still only ~ 0.04 per cent of the total SIMPLEX simulation volume, again too small to directly affect the ionization fronts and fractions at the locations where the high-ionization forbidden lines of interest form. Assuming He is neutral in the η_A wind at the start of the SIMPLEX simulations also allows us to more easily determine whether He-ionizing photons from η_B can penetrate the WWIRs and affect the pre-shock η_A wind. If so, the primary effect will be an increased fraction of He II in the innermost η_A wind, with little to no effect on the shape or extent of the He II ionization volume. Moreover, since η_B is thought to be an O- or WR-type star with $T_{\text{eff}} \simeq 36\,000$ – $41\,000$ K (Verner, Bruhweiler & Gull 2005; Hillier et al. 2006; Teodoro et al. 2008; Mehner et al. 2010), the number of photons it produces capable of ionizing He II to He III is effectively zero. Thus, there will be no He III region created by η_B beyond the WWIR zone, even if η_B 's radiation can penetrate the dense post-shock gas. Therefore, even for simulation Case C, the neglecting of η_A 's radiation is a justifiable simplification for the purposes of our work. The only caveat is that we do not account for any possible ionization of η_A 's pre-shock wind to He III by soft X-rays produced in the 420 km s^{-1} η_A shock. However, any such He III region near the WWIR zone at times around apastron is very likely to be negligible in extent, if it exists at all, as evidenced by the absence of any significant detectable He II $\lambda 4686$ emission in η

Car during its spectroscopic high state (Mehner et al. 2011; Teodoro et al. 2012).

Based on the above considerations, we neglect the η_A ionizing source in this work and focus on the influence of η_B .

2.3.2 The ionizing source η_B

For the RT calculations, we place a spherical ionizing source centred at the location of η_B . This ‘source’ is composed of a series of individual points randomly distributed about the sphere that defines the injection radius used in the SPH simulations for the wind of η_B ($30 R_\odot$). We use a total of 50 source points, which is large enough to result in a nearly isotropic photoionizing source. We find that using more points has little effect on the RT results. The total luminosity is divided among all 50 points, forming the nodes of the grid that emit radiation. These nodes are also capable of absorbing any radiation emitted by neighbouring points in the SIMPLEX grid. Based on the work of Mehner et al. (2010), Verner et al. (2005) and M12, we assume for η_B a total ionizing flux for hydrogen and helium of 3.58×10^{49} photons s^{-1} (3.02×10^{49} capable of ionizing H I and 5.62×10^{48} for ionizing He I), consistent with an O5 giant with $T_{\text{eff}} \approx 40\,000$ K (Martins, Schaerer & Hillier 2005).

3 RESULTS

To provide context for interpreting the RT results below, we begin with a brief description of the density and temperature structure of the system in the orbital plane for the Case A simulation (Fig. 3). Example number density slices in the xz and yz planes, plus number density slices in each plane for the Case B and C simulations, can be found in Figs 5, 7, and 9. Example slices showing temperature for each case can be found in M13. We focus on the Case A simulation as the \dot{M}_{η_A} assumed in this case most likely represents η_A ’s current observed mass-loss rate (Groh et al. 2012; M13).

Pittard et al. (1998), Pittard & Corcoran (2002), Okazaki et al. (2008), Parkin et al. (2009), Parkin et al. (2011), M12, and Russell (2013) showed that η_B is between the observer and η_A at apastron. Due to the highly eccentric binary orbit, η_B spends most of its time near apastron (right-hand side of panels in Fig. 3), so that the relatively undisturbed wind of η_A is located on the far (periastron) side of the system. Across every periastron passage, the hot and low-density wind of η_B pushes outward into the slow, high-density η_A wind, leading to the formation of a thin, high-density wall surrounding the lower density, trapped wind of η_B (Parkin et al. 2011; M13). This dense wall is accelerated to a velocity higher than the normal terminal velocity of η_A ’s wind and expands creating a thin, high-density sheet of trapped primary wind material. During periastron passage the arms of the WWIR become extremely distorted by orbital motion as the binary stars move towards their apastron positions. Moving back towards apastron, orbital speeds decrease and the η_B wind cavity regains its axisymmetric conical shape (Okazaki et al. 2008; Parkin et al. 2011; M13).

Dense arcs and shells of η_A wind visible in the outer regions on the apastron side of the system in the top panel of Fig. 3 highlight the fact that the binary has already undergone multiple orbits. Narrow cavities carved by η_B in η_A ’s dense wind during each periastron passage also exist on the periastron side of the system. Bordering these narrow cavities are the compressed, density-enhanced shells of primary wind formed as a result of the rapid wind–wind collision during each periastron.

While the periastron side of the system is dominated by the dense wind of η_A , the apastron side is dominated by the much lower-

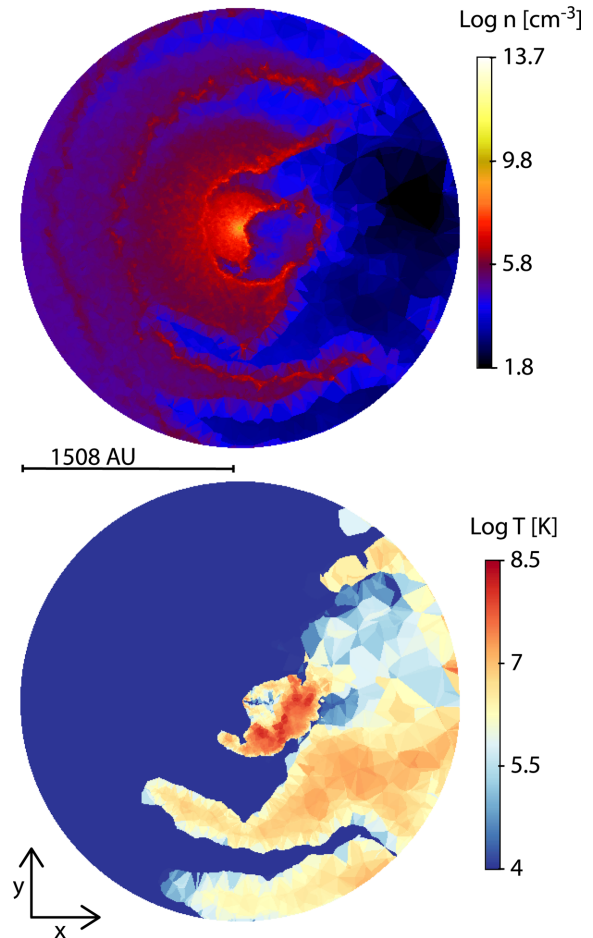


Figure 3. Slices in the xy orbital plane through the 3D simulation volume for the Case A simulation at apastron. The top plot shows the number density (log scale, cgs units), while the bottom shows log temperature (K). The lower density η_B wind is shock-heated by the wind–wind interaction to temperatures up to $\sim 10^{8.5}$ K. On the periastron (left-hand) side the denser η_A wind and compressed shells formed at periastron radiatively cool to $T \sim 10^4$ K.

density, faster wind of η_B , although arcs of compressed η_A wind also extend to the apastron side. These arcs are the remnants of the shells of η_A wind that flow in the apastron direction when η_B is at periastron (M13). The partially intact, most recent shell is visible just to the right of the centre of the image in the top panel.

There is also a clear temperature asymmetry between the apastron and periastron sides of the system (bottom panel of Fig. 3). The gas on the periastron side is much colder at $T \approx 10^4$ K. The various wind–wind collisions on the apastron side produce large volumes of gas shock-heated to temperatures between 10^6 and $10^{8.5}$ K. Because the gas on the apastron side is composed mostly of η_B wind material of low density, it cools slowly and adiabatically, allowing it to remain hot throughout the 5.54 yr orbital cycle. In contrast, the dense shells of post-shock primary wind cool radiatively very quickly down to $T \sim 10^4$ K (Parkin et al. 2011; M13). The innermost region of the system where the current WWIR is located, and the region where η_B ’s wind collides with the latest ejected shell of primary wind, have the highest temperatures and are responsible for the observed time-variable X-ray emission (Hamaguchi et al. 2007; Okazaki et al. 2008; Corcoran et al. 2010; Parkin et al. 2011).

3.1 The importance of collisional ionization

The bottom panel of Fig. 3 shows that the shocks induced by the violent wind–wind collisions heat the gas in the system to very high temperatures. Since the lower density material from η_B cools adiabatically, this gas remains extremely hot for most of the orbit, at temperatures well above those where collisional ionizations become important ($\gtrsim 10^6$ K). The collisional ionization fraction depends strongly on the temperature of the gas, which is in principle a function of the hydrodynamical motion, photoheating, and multiple cooling terms. In this initial study, as a first approximation, we use the temperature calculated by the SPH code to estimate the importance of collisional ionizations. In order to assess which process dominates, we performed a series of simulations with/without collisional-/photoionization. For brevity, we discuss here only the results for hydrogen for simulation Case A. Results for helium and Cases B and C are qualitatively similar.

Fig. 4 summarizes the results. The three panels represent the SIMPLEX output if we include, respectively, only collisional ionization, only photoionization, or both. For the only collisional ionization case, we assume collisional ionization equilibrium as an initial condition to the RT, as described in Section 2.2.2. In this case, the overall ionization structure unsurprisingly follows the plot of the temperature in Fig. 3. The cold, dense primary wind on the periastron side of the system, and the dense WWIRs of compressed primary wind that extend to the apastron side of the system (both in black in the first panel of Fig. 4), remain mostly neutral. However, hydrogen in the hot, lower density regions of shocked secondary wind are collisionally ionized (in blue and purple in the first panel of Fig. 4). The η_B wind in the outermost parts of the system is the most highly ionized due to the much lower density of the gas there, which results in less recombination. We also note in particular the two ‘fingers’ of highly ionized η_B gas that extend into the primary wind, located at the bottom of the panel. More importantly, we see that when only collisional ionizations are used, the dense WWIRs remain almost entirely neutral.

In the case of only photoionizations from η_B (middle panel of Fig. 4), mainly the lower-density η_B wind on the apastron side of the system is highly ionized (in yellow and orange). The lower density hot fingers of η_B wind trapped between the high-density walls of η_A wind show no ionization. These regions are effectively

shielded from the ionizing flux of η_B . Another important difference is the level of ionization in the η_B wind. Photoionizations are capable of reducing the fraction of neutral hydrogen by roughly four more orders of magnitude, compared to the case with only collisional ionization. Additionally, the η_B wind closest to the centre of the simulation is the most highly ionized since, even though the density is higher there, the material is much closer to the luminous ionizing source. This is the exact opposite of what was observed in the case of only collisional ionizations. We also see that photons from η_B are capable of penetrating the innermost wall of η_A wind material on the apastron side of the system, thus also highly ionizing it and the outer portions of η_B ’s wind. Detailed examination further shows that when photoionizations are used, the edges of the WWIRs facing η_B can be significantly ionized ($\log f_{H\text{I}} \lesssim -3$; Madura & Clementel, in preparation).

Using both collisional- and photoionizations results in a situation that resembles a superposition of the first two panels (right-hand panel of Fig. 4). The η_B wind on the apastron side remains highly ionized, but collisional ionization helps ionize the fingers of η_B wind located at the bottom of the panel. Interestingly, the $H\text{I}$ in the fingers is slightly more ionized now compared to the case with only collisional ionizations. This is because, due to the now reduced opacity caused by including collisional ionization, photons from η_B can more easily penetrate into the fingers and increase the overall level of ionization. A similar effect is seen in/near the WWIRs, which are also slightly more ionized when both collisional- and photoionizations are included, compared to the case with only photoionization. However, even when both collisional- and photoionizations are used, the dense η_A wind on the periastron side of the system remains neutral.

Given all of these results, we consider both collisional- and photoionizations as necessary for any proper RT simulations of η Car. The remainder of the results in this paper are based on simulations that accordingly incorporate both.

3.2 Overall ionization structure and influence of \dot{M}_{η_A}

3.2.1 The orbital plane

The top row of Fig. 5 shows the SIMPLEX number density in the orbital plane for simulation Cases A–C. As demonstrated by M13,

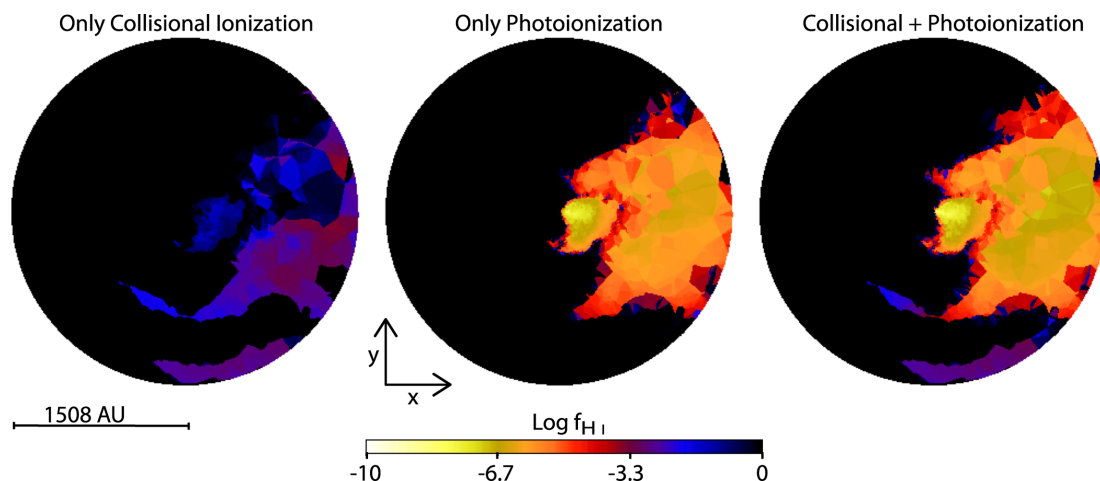


Figure 4. Slices in the xy orbital plane through the 3D SIMPLEX simulation volume for Case A at apastron showing the logarithm of the fraction of neutral hydrogen assuming Left: collisional ionization only, Centre: photoionization only, and Right: collisional- and photoionization. Including collisional ionization is necessary to ionize the small cavities in the primary wind and the ‘fingers’ of low-density η_B wind trapped between the higher density walls of η_A wind that form around periastron.

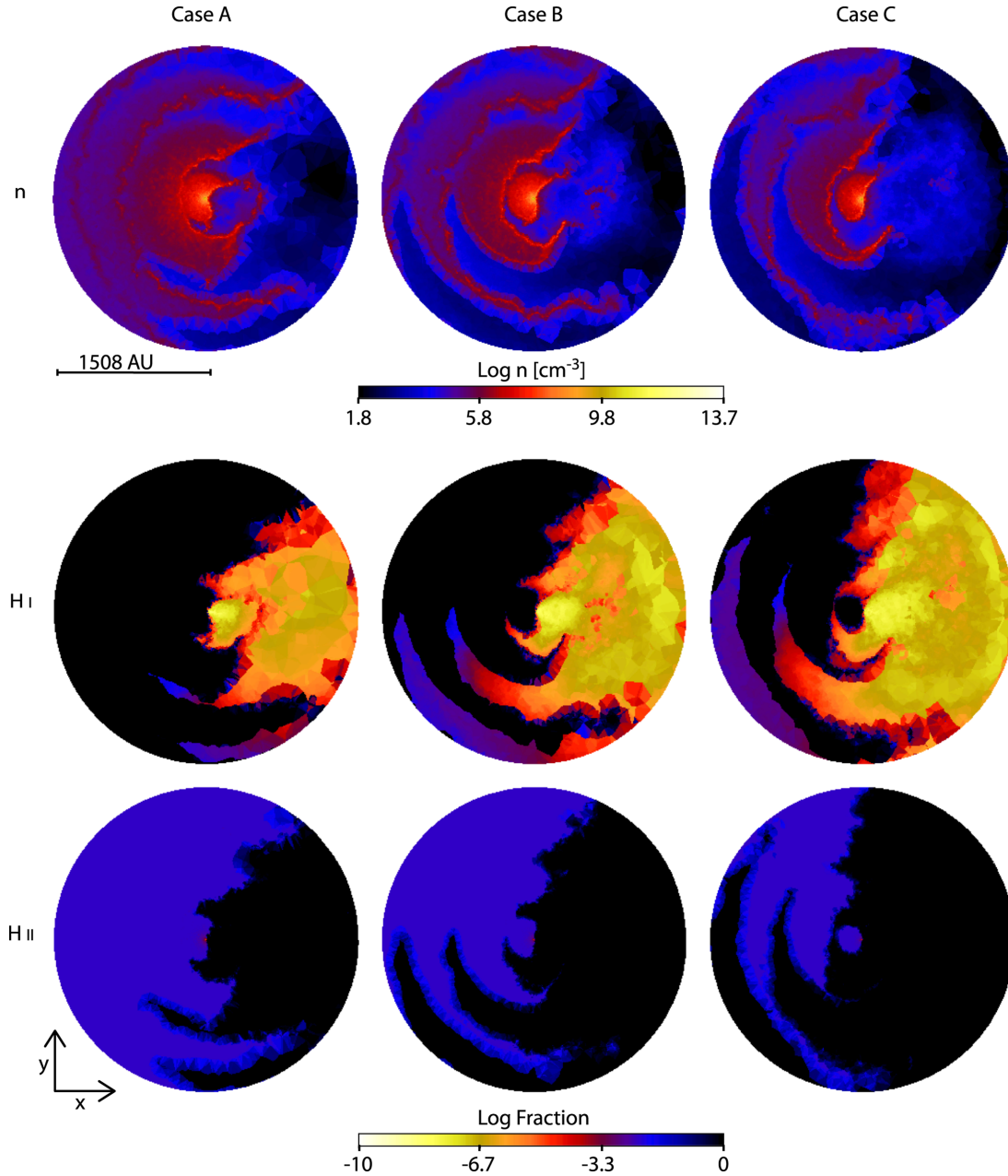


Figure 5. Slices in the xy orbital plane through the 3D SIMPLEX simulation volume for the three different assumed \dot{M}_{η_A} . Columns illustrate, from left to right, Cases A to C. Rows show, from top to bottom, the SIMPLEX number density (log scale, cgs units) and the computed fractions of H I and H II (log scale).

\dot{M}_{η_A} determines the overall shape of the WWIRs and the stability of the arcuate shells expanding on the apastron side of the system. Lowering \dot{M}_{η_A} increases the opening angle of the shock cone created by η_B , increasing the volume of low-density η_B wind. This is particularly noticeable in the size of the low-density fingers of η_B wind that strongly reduce the volume of unperturbed primary wind. The lower the \dot{M}_{η_A} , the wider and more extended the fingers. In Cases B and C, the fingers extend to the back (periastron) side of η_A 's wind. The dense shells of η_A wind on the apastron side are also more stable and remain intact longer for higher values of \dot{M}_{η_A} (M13). As a consequence, we expect that the 3D shape, position, intensity, and variability of the ionization depend strongly on \dot{M}_{η_A} .

The middle and bottom rows of Fig. 5 present, respectively, the computed fractions of H I and H II in the orbital plane. The WWIRs and high-density walls surrounding the lower density

trapped wind of η_B define the separation between the neutral and ionized-hydrogen regions. These high-density η_A wind structures are able to trap the hydrogen ionizing photons from η_B . We also see that as \dot{M}_{η_A} decreases, the volume of ionized hydrogen increases greatly on both the apastron and periastron sides of the system. The larger fingers for Cases B and C allow the ionizing radiation from η_B to penetrate into the low-density cavities that are carved within the back side of the primary wind every periastron passage.

In the H II maps of Fig. 5 it is possible to see a large fraction of neutral hydrogen at and to the periastron side of η_A . As described in Section 2.3.1, in reality, the hydrogen in this inner region should be ionized by η_A out to a radius of ~ 120 au in Cases A and B, and everywhere in Case C. However, the absence of an η_A ionizing source in our simulations prevents this from occurring. Nonetheless, the absence of an η_A source in our simulations reveals an important

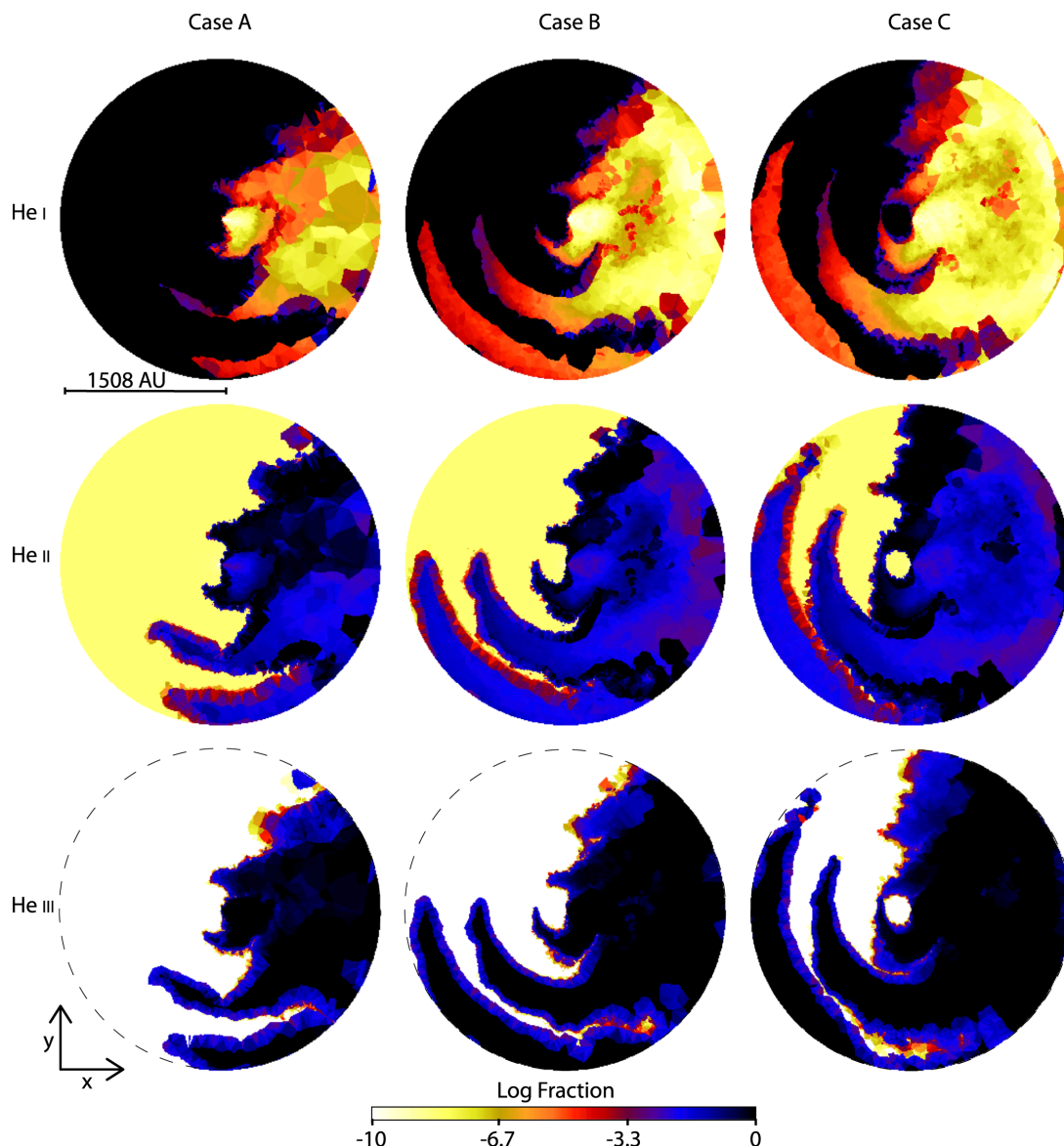


Figure 6. Same as Fig. 5, but with rows showing, from top to bottom, the computed fractions of He I, He II and He III (log scale). In this and future plots of He III, the dashed circle marks the edge of the spherical computational domain.

result that may otherwise be missed, namely, that the high optical depth of the inner WWIR prevents any η_B ionizing photons from penetrating into the inner η_A wind. The lack of any regions of ionized hydrogen in the unshocked primary wind on the periastron side of the system implies that regardless of the ionization structure of η_A 's innermost wind, ionizing photons from η_B cannot penetrate the inner WWIR or significantly affect the dense η_A wind on the periastron side of the system at times around apastron.

Fig. 6 illustrates the fractions of He I, He II and He III in the orbital plane for the three \dot{M}_{η_A} simulations. Comparing to Fig. 5, we see that the regions of He III correlate strongly with the regions of H II. As expected, the regions of H I and He I are also correlated. The fully-ionized nature of helium in the lower density η_B wind is due to the presence of large volumes of very high temperature shocked gas, plus the relatively close proximity of such gas to the hot, luminous η_B ionizing source. As with hydrogen, the helium in the denser primary wind is neutral. The trends as a function of \dot{M}_{η_A} seen in Fig. 5 for the hydrogen ionization structure are also apparent in the

plots of He I and He III. This is a key result, as it implies that even with the lower \dot{M}_{η_A} of Case C, η_B 's He-ionizing radiation cannot penetrate significantly the dense WWIRs.

The structure of He II (middle row of Fig. 6) is more involved than that of He I and He III. Interestingly, significant fractions of He II are principally located in the high-density walls of the WWIRs and outer edges of the dense fingers of η_A wind that define the low-density fingers of η_B wind. Regions of lower temperature unshocked η_B wind also consist of mostly He II. The He II is seen primarily as a marker for the transition between the regions of He I and He III. For this reason, He II appears to be an excellent tracer for the high-density compressed post-shock η_A gas.

3.2.2 The xz and yz planes

To help the reader more fully appreciate the complex 3D structure of the simulation results, Figs 7–10 present slices showing the number density and H and He ionization structures in the xz and yz planes

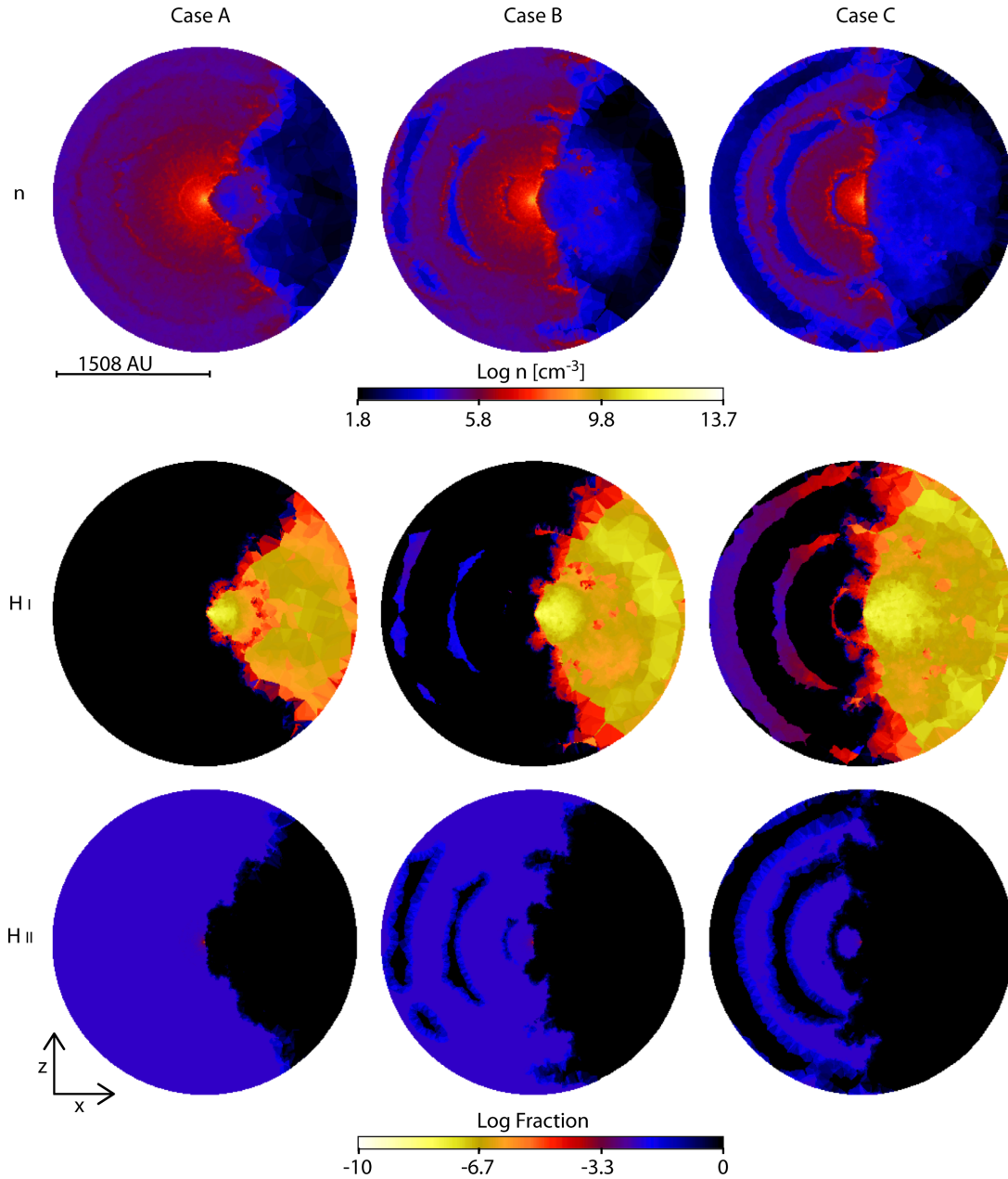


Figure 7. Same as Fig. 5, but for slices centred in the xz plane.

for each \dot{M}_{η_A} . The differences in ionization structure between the three \dot{M}_{η_A} are even more apparent in these two planes. There is a clear left–right asymmetry in the density and ionization structure in each panel of the figures. As in Figs 5 and 6, the regions of He III correlate strongly with the regions of H II, while regions of He I correlate with those of H I. The overall volume of ionized material increases with decreasing \dot{M}_{η_A} .

Fig. 7 shows that the higher the value of \dot{M}_{η_A} , the smaller the wind cavities carved by η_B on the left-hand (periastron) side of the system. They are practically invisible for Case A. As a result, hydrogen and helium both appear neutral on the left in the Case A panels. Only the large η_B wind cavity on the apastron side of the system is ionized in Case A. Figs 7 and 8 illustrate how the wind cavities on both the periastron and apastron sides of the system are much larger and remain hot for Cases B and C, resulting in well-defined regions of ionized hydrogen and helium.

The top row of Fig. 7 also shows clear differences with \dot{M}_{η_A} in the density and fragmentation of the dense shell of η_A wind material on the right-hand (apastron) side of the system. In Case A, the dense shell is more or less intact, while in Cases B and C it has fragmented considerably and started to mix with the lower density η_B wind. This fragmenting shell produces an interesting hydrogen ionization structure on the right-hand (apastron) side of the system that consists of an inner and outer region of low-density, highly ionized η_B wind (in yellow/orange, middle row of Fig. 7) separated by a diffuse shell of denser, less-ionized η_A wind (in red). The middle row of Fig. 8 again shows that the He II is located in the high-density walls of the WWIRs and outer edges of the dense fingers of η_A wind that define the low-density fingers of η_B wind, thus tracing the compressed post-shock η_A gas.

Fig. 9 shows that the cavities carved on the right-hand (+y) side are always smaller than the ones carved on the left-hand (−y),

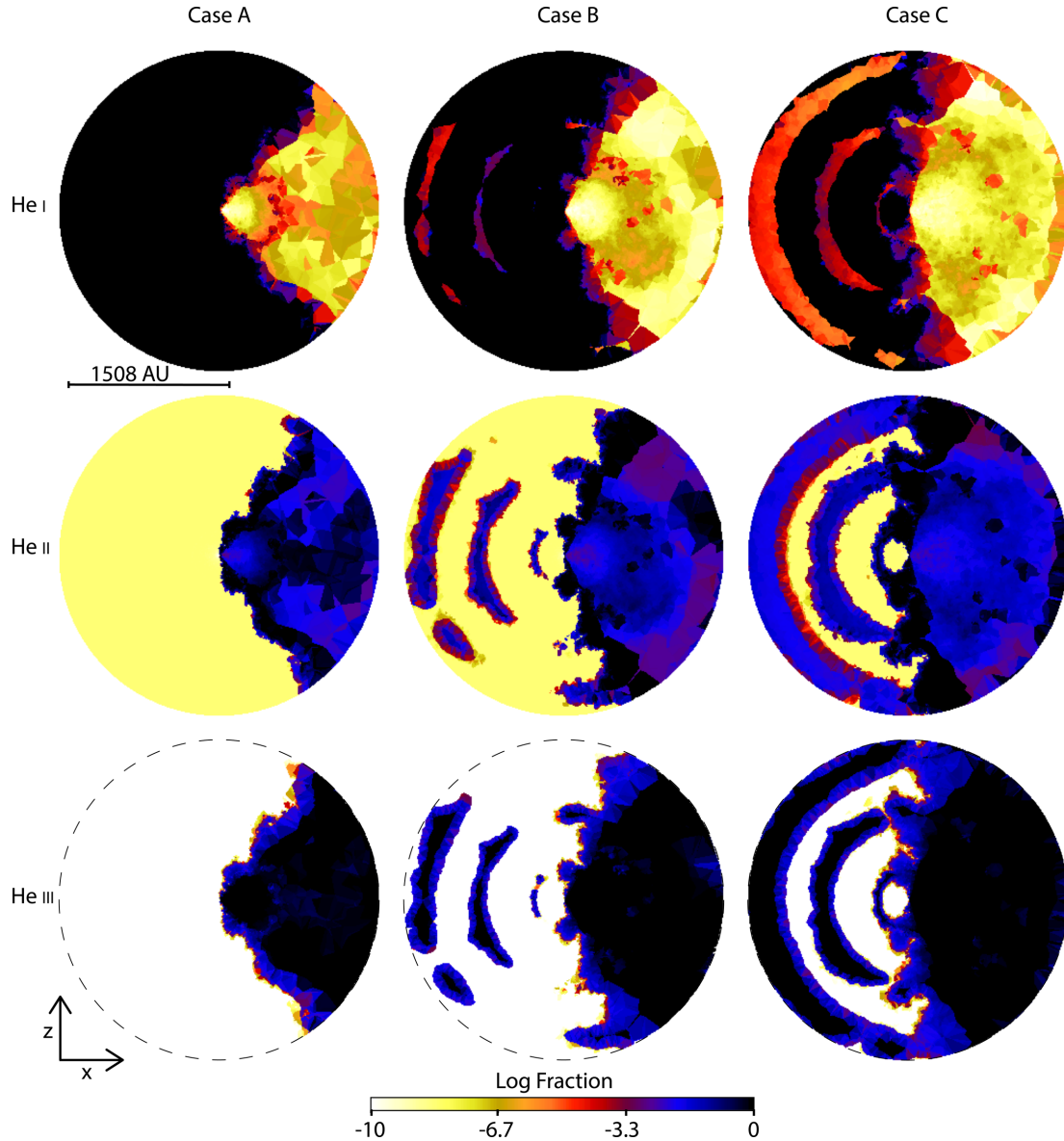


Figure 8. Same as Fig. 6, but for slices centred in the xz plane.

regardless of the value of \dot{M}_{η_A} . However, the difference in cavity size between the $+y$ and $-y$ sides increases with decreasing \dot{M}_{η_A} . The larger cavities on the left-hand ($-y$) side are also hotter, resulting in well-defined regions of ionized H and He concentrated on the left-hand side. Finally, we see that the shells of dense, compressed η_A wind on the left are thicker and remain intact longer the higher the \dot{M}_{η_A} , reducing the overall volume of ionized material. We note that in reality, H should be ionized everywhere in Case C.

4 DISCUSSION

A major goal of this work was to improve upon the simple approach of M12 for computing the highly ionized regions in the η Car system where various observed forbidden emission lines form. The ionization volumes in M12 were based on geometrical criteria combined with a density threshold, and considered only photoionization of hydrogen due to η_B . Fig. 11 shows an example of the photoionization region in the orbital plane for Case A at a phase near apastron, computed using the methods of M12. The result is

a rather large Strömgen-sphere-like volume that predicts the distance that H I ionizing photons from η_B can travel. Comparing this to the SIMPLEX results in Figs 5 and 6, we clearly see that the SIMPLEX method does a significantly improved job at computing the detailed structure of the various ionization volumes, including the penetration of η_B 's photons into the fingers of low-density wind carved within the optically-thick wind of η_A . The approach of M12 does not account for the extended WWIR arcs on the apastron side and thus overestimates the ionization extent in these regions.

Effects due to collisional ionization and recombination were also not considered by M12. In addition to missing details in the ionization of the low-density fingers of η_B wind on the apastron side, subtle variations in the ionization of η_A 's wind and the WWIRs on the periastron side, due to recombination, are also absent in the M12 results. More importantly, the M12 model does not compute any ionization fractions. The ion fraction is estimated using tables and assuming collisional ionization equilibrium. In contrast, the SIMPLEX method computes detailed ionization fractions for both hydrogen and helium. This provides estimates of the extent and magnitude of the

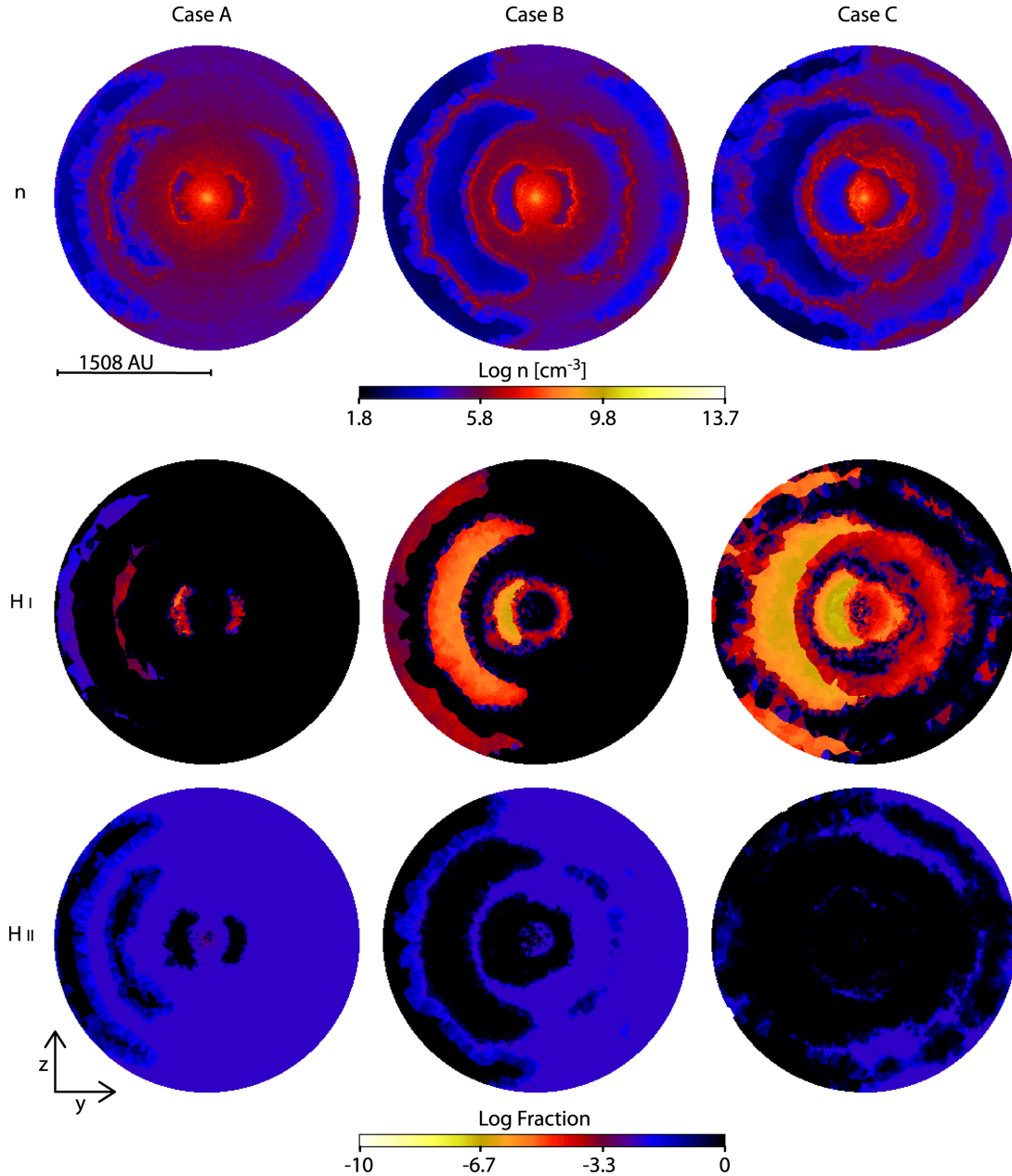


Figure 9. Same as Fig. 5, but for slices centred in the yz plane.

ionization as a function of energy, previously unavailable information that is important for determining where the forbidden lines of different ionization potential form. Such information is also crucial for placing constraints on η_B 's ionizing flux.

M12 found that the observed broad forbidden line emission (Gull et al. 2009, 2011) depends strongly on \dot{M}_{η_A} and the ionizing flux from η_B . M13 suggested that if the flux from η_B remains constant, but \dot{M}_{η_A} drops by a factor of 2 or more from an initial value of $\approx 8.5 \times 10^{-4} M_{\odot} \text{ yr}^{-1}$, then the photoionization region created by η_B should increase considerably in size. The results of the SIMPLEX simulations in Figs 5–10 confirm this, implying that any recent decrease in \dot{M}_{η_A} (as speculated by e.g. Mehner et al. 2010, 2011, 2012) should greatly change the spatial extent, location, and flux of the observed broad high-ionization forbidden emission lines. The results of this paper will be used in future work to compute

synthetic slit-spectral observations of various forbidden lines (e.g. [Fe II], [Fe III]) for comparison to recent (Gull et al. 2011; Teodoro et al. 2013) and planned observations of η Car from *HST*/STIS. Comparison of the synthetic and observational data can be used to place additional constraints on any recent changes in \dot{M}_{η_A} , important for determining η Car's near- and long-term fates (M13). The improved SIMPLEX models will also be useful for refining the orbital orientation parameters obtained by M12, and possibly also the stellar wind parameters and/or wind momentum ratio.

5 SUMMARY AND CONCLUSION

We showed that using SIMPLEX for the post-processing of 3D SPH simulation output is a viable method to investigate the ionization state of the gas in a complicated colliding wind binary like η Car.

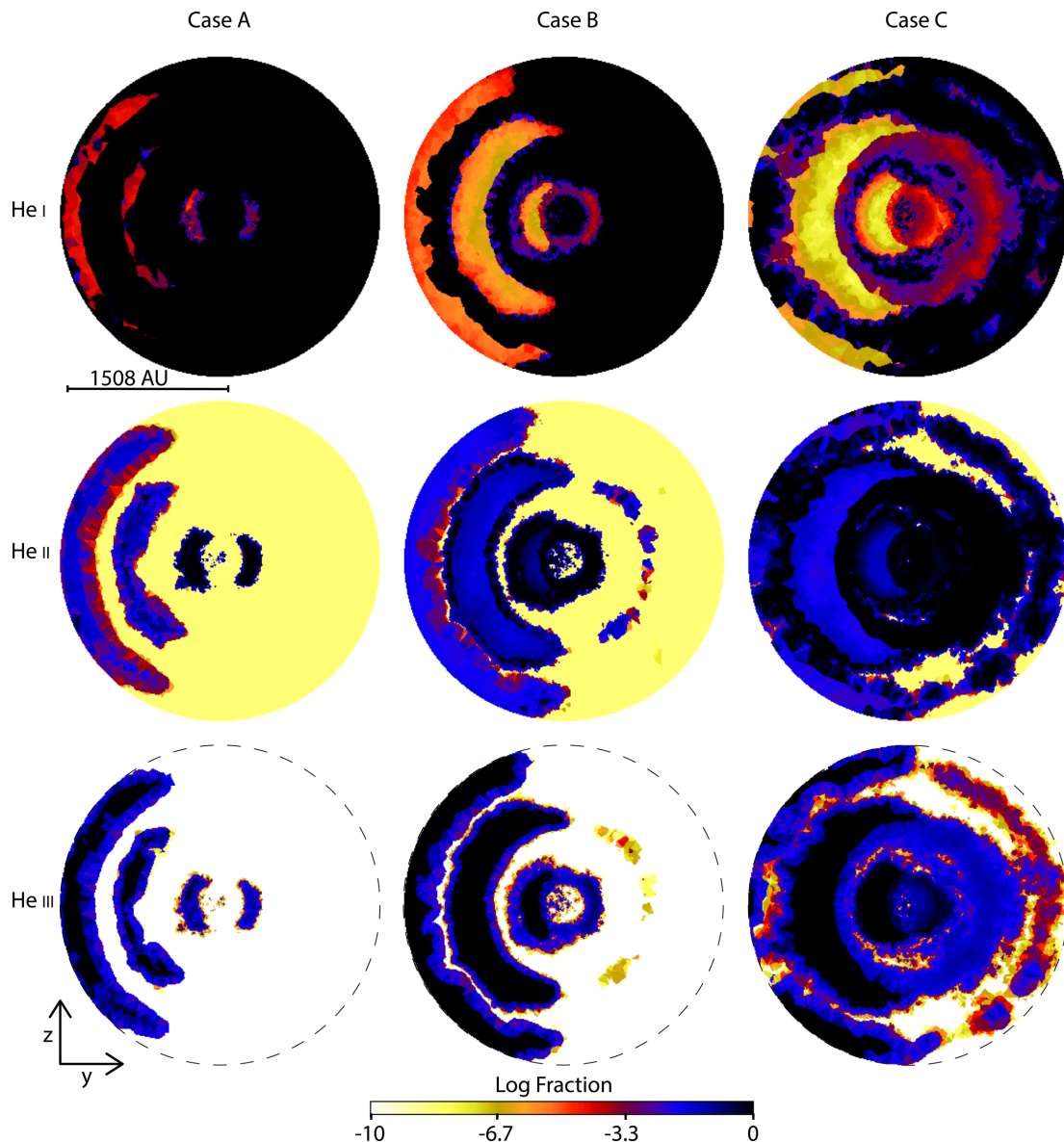


Figure 10. Same as Fig. 6, but for slices centred in the yz plane.

SIMPLEX provides detailed 3D results of the ionization volumes and fractions for various species of interest, in this case hydrogen and helium, and improves greatly upon simpler approaches such as that in M12. Below, we summarize our most important results.

(1) The unstructured SIMPLEX mesh reproduces everywhere the features present in the original 3D SPH simulation data, leading to a density map that is in excellent agreement with the original SPH one, even where sharp gradients are present. SIMPLEX also preserves the high spatial resolution of the original SPH data.

(2) The inclusion of collisional ionization changes the ionization structure of hydrogen and helium most notably in the underdense fingers of η_B wind that form between the dense shells of η_A wind created every periastron passage. Since these regions are typically shielded from η_B 's ionizing flux, including collisional ionization is important to achieve a more complete description of the total ionized volume.

(3) Collisional ionization is important in reducing the total optical depth within regions composed of hot η_B wind that are heated

to high temperatures by the various wind–wind collisions. This increases the efficiency of photoionization by η_B , allowing portions of the dense areas of post-shock η_A wind and WWIRs on the apastron side of the system to be ionized to varying degrees.

(4) The SIMPLEX simulations show that the dense, innermost WWIR prevents the η_B ionizing radiation from penetrating far into the inner wind of η_A . At phases near apastron, hydrogen and helium ionization are concentrated on the apastron side of the system, with the periastron side consisting of mostly neutral η_A wind. However, as \dot{M}_{η_A} is decreased, low-density fingers of ionized η_B wind penetrate the dense η_A wind on the periastron side.

(5) We find regions of He III correlate strongly with regions of H II, while regions of H I strongly correlate with those of He I. He II is more complex and primarily marks the transition between the regions of He I and He III. He II appears to be an excellent tracer for the dense, compressed post-shock η_A gas and WWIRs.

(6) Changing \dot{M}_{η_A} results in quite different ionization volumes, with much more ionized gas present for lower \dot{M}_{η_A} . Significant variations in ionization structure due to changes in \dot{M}_{η_A} are

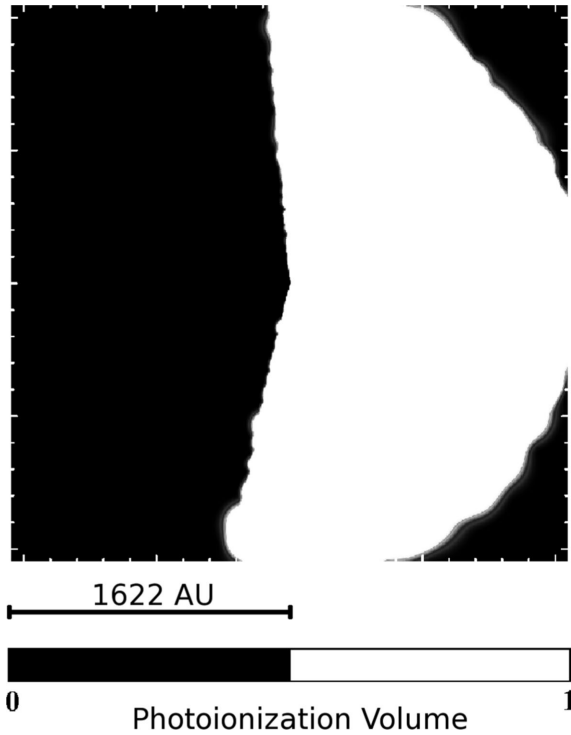


Figure 11. Slice in the xy orbital plane showing the hydrogen photoionization region created by η_B (white = ionized) for the Case A simulation at apastron, computed using the approach in M12.

clearly apparent in the xz and yz planes as well as the orbital plane.

(7) The large apparent changes in ionization volume with decreasing \dot{M}_{η_A} imply that any major decrease in \dot{M}_{η_A} should lead to significant observable changes in the spatial extent, location, and flux of the broad high-ionization forbidden emission lines. Future models based on the *SIMPLEX* results may be used to constrain any such potential changes.

In addition to helping us understand η Car's recent mass-loss history, the past (Gull et al. 2011; Teodoro et al. 2013) and future *HST*/STIS spatial maps of η Car's high-ionization forbidden emission lines are a powerful tool that can potentially be used to better determine the nature of the unseen companion star η_B . Specifically, detailed 3D models of the forbidden line emission based on *SIMPLEX* results like those presented here may allow us to place tighter constraints on η_B 's ionizing flux. This could then be compared to stellar models for a range of O (Martins et al. 2005) and WR (Crowther 2007) stars, providing a more accurate estimate of η_B 's luminosity and temperature.

While applied here to the specific case of η Car, *SIMPLEX* can be used to study numerous other colliding wind binaries or similar systems of astrophysical interest. Application of the *SIMPLEX* algorithm is also not limited to the post-processing of SPH simulation data, output from grid-based codes that use adaptive mesh refinement may also be analysed using *SIMPLEX* (Kruip 2011). And although *SIMPLEX* has been used in this paper to post-process hydrodynamical simulation data, this work helps set the stage for a future coupling of *SIMPLEX* with the SPH method in order to perform 3D time-dependent radiation-hydrodynamics simulations of complex astrophysical phenomena (see e.g. Pelupessy et al. 2013).

ACKNOWLEDGEMENTS

TIM is supported by an appointment to the NASA Postdoctoral Program at the Goddard Space Flight Center, administered by Oak Ridge Associated Universities through a contract with NASA. Support for TRG was through programs #12013, 12508, 12750, 13054, and 13395, provided by NASA through a grant from the Space Telescope Science Institute, which is operated by the Association of Universities for Research in Astronomy, Inc., under NASA contract NAS 5-26555.

REFERENCES

- Corcoran M. F., Ishibashi K., Swank J. H., Petre R., 2001, *ApJ*, 547, 1034
 Corcoran M. F., Hamaguchi K., Pittard J. M., Russell C. M. P., Owocki S. P., Parkin E. R., Okazaki A., 2010, *ApJ*, 725, 1528
 Crowther P. A., 2007, *ARA&A*, 45, 177
 Damineli A., Conti P. S., Lopes D. F., 1997, *New. Astron.*, 2, 107
 Damineli A. et al., 2008a, *MNRAS*, 384, 1649
 Damineli A. et al., 2008b, *MNRAS*, 386, 2330
 Davidson K., Humphreys R. M., 1997, *ARA&A*, 35, 1
 Fahed R. et al., 2011, *MNRAS*, 418, 2
 Ferland G. J., Korista K. T., Verner D. A., Ferguson J. W., Kingdon J. B., Verner E. M., 1998, *PASP*, 110, 761
 Franco J., Tenorio-Tagle G., Bodenheimer P., 1990, *ApJ*, 349, 126
 Gayley K. G., Owocki S. P., Cranmer S. R., 1997, *ApJ*, 475, 786
 Groh J. H. et al., 2010, *A&A*, 517, A9
 Groh J. H., Hillier D. J., Madura T. I., Weigelt G., 2012, *MNRAS*, 423, 1623
 Gull T. R. et al., 2009, *MNRAS*, 396, 1308
 Gull T. R., Madura T. I., Groh J. H., Corcoran M. F., 2011, *ApJ*, 743, L3
 Hamaguchi K. et al., 2007, *ApJ*, 663, 522
 Henley D. B., Corcoran M. F., Pittard J. M., Stevens I. R., Hamaguchi K., Gull T. R., 2008, *ApJ*, 680, 705
 Hillier D. J., Davidson K., Ishibashi K., Gull T., 2001, *ApJ*, 553, 837
 Hillier D. J. et al., 2006, *ApJ*, 642, 1098
 Kruip C., 2011, PhD thesis, Univ. Leiden
 Kruip C. J. H., Paardekooper J.-P., Clauwens B. J. F., Icke V., 2010, *A&A*, 515, A78
 Lefèvre L. et al., 2005, *MNRAS*, 360, 141
 Madura T. I., Groh J. H., 2012, *ApJ*, 746, L18
 Madura T. I., Gull T. R., Owocki S. P., Groh J. H., Okazaki A. T., Russell C. M. P., 2012, *MNRAS*, 420, 2064 (M12)
 Madura T. I. et al., 2013, *MNRAS*, 436, 3820 (M13)
 Martins F., Schaerer D., Hillier D. J., 2005, *A&A*, 436, 1049
 Mehner A., Davidson K., Ferland G. J., Humphreys R. M., 2010, *ApJ*, 710, 729
 Mehner A., Davidson K., Martin J. C., Humphreys R. M., Ishibashi K., Ferland G. J., 2011, *ApJ*, 740, 80
 Mehner A., Davidson K., Humphreys R. M., Ishibashi K., Martin J. C., Ruiz M. T., Walter F. M., 2012, *ApJ*, 751, 73
 Monnier J. D., Tuthill P. G., Danchi W. C., 1999, *ApJ*, 525, L97
 Okazaki A. T., Owocki S. P., Russell C. M. P., Corcoran M. F., 2008, *MNRAS*, 388, L39
 Osterbrock D. E., Ferland G. J., 2006, *Astrophysics of Gaseous Nebulae and Active Galactic Nuclei*, 2nd edn. University Science Books, Mill Valley, CA
 Owocki S., 2007, in St.-Louis N., Moffat A. F. J., eds, *ASP Conf. Ser. Vol. 367, Massive Stars in Interactive Binaries*. Astron. Soc. Pac., San Francisco, p. 233
 Paardekooper J.-P., Kruip C. J. H., Icke V., 2010, *A&A*, 515, A79
 Paardekooper J.-P., Pelupessy F. I., Altay G., Kruip C. J. H., 2011, *A&A*, 530, A87
 Parkin E. R., Sim S. A., 2013, *ApJ*, 767, 114
 Parkin E. R., Pittard J. M., Corcoran M. F., Hamaguchi K., Stevens I. R., 2009, *MNRAS*, 394, 1758
 Parkin E. R., Pittard J. M., Corcoran M. F., Hamaguchi K., 2011, *ApJ*, 726, 105

- Pawlik A. H., Schaye J., 2008, MNRAS, 389, 651
- Pelupessy F. I., van Elteren A., de Vries N., McMillan S. L. W., Drost N., Portegies Zwart S. F., 2013, A&A, 557, A84
- Pittard J. M., Corcoran M. F., 2002, A&A, 383, 636
- Pittard J. M., Stevens I. R., Corcoran M. F., Ishibashi K., 1998, MNRAS, 299, L5
- Ritzerveld N. G. H., 2007, PhD thesis, Univ. Leiden
- Ritzerveld J., Icke V., 2006, Phys. Rev. E, 74, 026704
- Russell C. M. P., 2013, PhD thesis, Univ. Delaware
- Shapiro P. R., Iliev I. T., Alvarez M. A., Scannapieco E., 2006, ApJ, 648, 922
- Smith N., 2006, ApJ, 644, 1151
- Stevens I. R., Pollock A. M. T., 1994, MNRAS, 269, 226
- Teodoro M., Daminieli A., Sharp R. G., Groh J. H., Barbosa C. L., 2008, MNRAS, 387, 564
- Teodoro M. et al., 2012, ApJ, 746, 73
- Teodoro M., Madura T. I., Gull T. R., Corcoran M. F., Hamaguchi K., 2013, ApJ, 773, L16
- Townsend R. H. D., 2009, ApJS, 181, 391
- Tuthill P. G., Monnier J. D., Danchi W. C., 1999, Nature, 398, 487
- Verner E., Bruhweiler F., Gull T., 2005, ApJ, 624, 973
- Whitelock P. A., Feast M. W., Marang F., Breedt E., 2004, MNRAS, 352, 447
- Williams P. M., Rauw G., van der Hucht K. A., 2009, MNRAS, 395, 2221

This paper has been typeset from a \LaTeX file prepared by the author.